Amorphous Dielectric Metal-Organic Electron Injection Layer for Efficient Inverted Organic Light-Emitting Diodes

*Lina Sun**[1], *Tsukasa Yoshida*[2], *Yuya Harada*[2], *Matthew Schuette White*[3] *and Yoshiyuki Suzuri*[1]

[1]Innovation Center for Organic Electronics (INOEL), Yamagata University, Arcadia 1-808-48, Yonezawa, Yamagata 992-0119, Japan

[2] Graduate School of Science and Engineering, Yamagata University, Jonan 4-3-16, Yonezawa, Yamagata 992-8510, Japan

[3] Department of Physics and Materials Science Program, University of Vermont, Burlington, VT 05405-0125, USA

Corresponding Author

*E-mail: sunlina@yz.yamagata-u.ac.jp

Abstract: Solution processed metal organic thin film was found to act as an efficient and stable electron injection layer (EIL) in inverted organic light emitting diodes (iOLEDs). Mild annealing of zinc(II) methoxyethoxide (ZME) under N_2 resulted in nanocrystals of ZnO (nc-ZnO) within highly compact amorphous gel of ZME (ag-ZME). While well-crystallized ZnO caused a strong electron leakage to reduce device efficiency, the ag-ZME processed at a temperature as low as 30°C did work efficiently. DC capacitance analysis revealed a highly dielectric behavior of ag-ZME that achieves selective electron injection to the emission layer, while preventing non-emissive direct reduction of hole, unlike crystalline ZnO with intra-band defect states to cause electron leakage. We also employed calcium(II) methoxyethoxide (CME) as an EIL and demonstrated almost the same performance in iOLEDs. The 4s orbitals of Ca(II) and Zn(II) in ag-CME and ag-ZME are used to regulate the electron injection, whereas the redundantly high conductivity of crystalline ZnO can only reduce the efficiency. The iOLED with a balanced nc-ZnO/ag-ZME by annealing at 100°C achieved a high current efficiency of 25.5 cd A^{-1} and an operating half-life stability exceeding 2000 h @100 cd m^{-2}, appealing for its practical use in iOLEDs.

Keywords: organic light-emitting diode, electron injection layer, zinc oxide, metal-organic, solution process, dielectric material

1. Introduction

Organic light emitting diodes (OLEDs) for advanced displays and lightings can potentially be fabricated by low temperature solution processing onto flexible substrates with large areas at low cost [1-5]. For their practical use, however, stability improvements and alternative architectures will enable new applications and form-factors. While high barrier coating to encapsulate the entire device is a pathway to improve stability [6-10], the device structure can also be modified.

Conventional-architecture OLEDs are in bottom-anode structures, thus employ highly-reactive low-work-function metals such as Al and Ca as top cathode contacts. Delamination of such metal contacts by their

oxidation is often the cause of degradation [11]. Bottom-cathode structures, known as inverted OLEDs (iOLEDs), are therefore proposed to allow use of stable noble metals with high work functions, such as Au and Ag, for the top anodes. Improved stabilities have been claimed for iOLEDs developed by several groups [12-15].

One of the biggest challenges in successful development of iOLEDs is to find good materials for electron injection layers (EILs) to be coated onto the transparent bottom cathode, preferably by mild processing compatible with Sn-doped In_2O_3 (ITO) coated conductive plastic films [15-19]. Unlike the established Al/LiF top contacts for conventional OLEDs [20, 21], transparent alternative EILs at the bottom of iOLEDs often limit the efficiency of the device [22-25]. Some researchers attribute the limitations to electron transport [13, 16], whereas the others propose electron injection as the dominant factor [15, 18-21].

Zinc oxide (ZnO) is commonly seen as one of the best materials for the bottom contacts in iOLEDs, for its excellent electron mobility, optical transparency, chemical stability and low temperature processability [17-19]. An important lesson from prior studies of iOLEDs employing ZnO is the need of modification of ZnO surface to realize high efficiency. The device efficiencies were often largely improved by coating ZnO with polyethyleneimine (PEI) [18, 26, 27] and self-assembled monolayer adsorption of organic molecules with controlled dipole moments [19, 28-30]. These organic modifiers are not conductive, which indicates that electron transport is not the limiting process in the efficiency of ZnO. Some authors claimed matching of work function of ZnO by organic modifiers as the reason for efficient electron injection [19, 26, 28, 30].

With the above-mentioned backgrounds in mind, we have explored possibilities to employ low-temperature solution processed metal oxides as EILs for iOLEDs. Here, we employed a novel complex of Zn(II)methoxyethoxide (ZME) as zinc precursor for the preparation of ZnO thin films. The iOLED devices employing the ZME strongly converted into crystalline ZnO (nc-ZnO) by relative high

temperature (> 130°C) annealing indeed gave high current but weak emission, whereas those partially converted into nc-ZnO or simply dried to amorphous gel of ZME (ag-ZME) by mild heat treatment performed very well. Specifically, the iOLEDs showed small current accompanied with strong emission owing to efficient electron injection. The devices were analyzed for their DC capacitance, which indicated dielectric behavior of ag-ZME as the key factor for the efficiency improvement.

In this paper, characterizations of thus prepared nc-ZnO/ag-ZME hybrid layers and results of device analysis are presented to discuss the prerequisites of EILs in high performance iOLEDs. The results show that the high conductivity of ZnO may not be advantageous for EILs, instead leading to a new vision and design strategy for iOLEDs. The characteristics of the iOLEDs employing the ZME-based EILs are also compared with those of the vacuum-processed OLED in conventional architecture employing the same EML. Long-term stability of the newly-developed iOLED has also been tested to demonstrate practical usability of ZME-based materials.

2. Experimental section

2.1 Thin film preparation

ZME or CME layers were prepared from solutions of zinc methoxyethoxide (Alfa Aesar, 5% w/v) or calcium methoxyethoxide (Alfa Aesar, 20% w/v) in 2-methoxyethanol. The solutions were appropriately diluted with 2-methoxyethonal anhydrous (2-ME, Sigma-Aldrich, 99.8%) to control the layer thickness. The solutions were spin-coated onto substrates at 6,000 rpm for 30 s, employing a Mikasa MS-A150 spin-coater, and heated at 30, 60, 100, 130 and 200°C for 1 h, as the samples are denoted as T30, T60, T100, T130 and T200, respectively. All of these processes were done in an N_2-filled glovebox (O_2, H_2O < 10 ppm) at room temperature. Si single crystal wafer of (100) cut was used as the substrate for most of characterizations, whereas a quartz glass plate was used for UV-vis absorption and PL measurements.

2.2 Thin film characterizations

The film thickness and refractive index (n at 800 nm) were measured on a J.A. Woollam VASE 32 spectroscopic ellipsometer. UV-vis absorption spectra were measured on a JASCO, V-570 spectrophotometer. Photoluminescence (PL) spectra were measured on a JASCO, FP6600 spectrophotometer at room temperature under air. The film samples were placed with their plane in 30º angle with respect to the excitation beam. No cut-off filters were used as they were not needed under the measuring conditions used in this study. The surface morphology was observed by an atomic force microscope (AFM, Hitachi High-Tech. Science Corp. SPI3800N/SPA500) in dynamic force mode, which also allowed determination of surface roughness. High resolution transmission electron microscope (HR-TEM) images were obtained by a JEOL, JEM-2100F for the samples prepared by casting the ZME solution onto a microgrid supported by Cu mesh (Ouken) and applying the same heat treatment as the film samples, which resulted in approximately 30 nm thickness of the layers. X-ray photoelectron spectroscopy (XPS) measurements were carried out in Sumika Chemical Analysis Service (SCAS) Ltd. using a Thermo Fisher Scientific, K-Alpha^{+} using monochromatic Al Kα X-ray source.

2.3 Device fabrication and characterization

Inverted OLEDs were fabricated as follows. ZME or CME layers were fabricated on patterned indium tin oxide (ITO) coated glass substrates (Atsugi Micro) according to the procedure described above. They were transferred to a vacuum chamber without exposure to air for sequential deposition of organic layers and eventually Al top electrode by vacuum evaporation. The structure of thus prepared iOLEDs are as ITO cathode (110 nm) / ZME or CME layers as EIL /2,9-dinaphthalen-2-yl-4,7-diphenyl-1,10-phenanthroline (NBP) (35 nm) as ETL / 4,4-bis(N-carbazolyl)-1,1-biphenyl (CBP) doped with 6% of $Ir(ppy)_3$ (35 nm) as EML / N,N-di(1-naphthyl)-N,N-diphenyl-(1,1-biphenyl)-4,4-diamine (NPD) (25 nm) as HTL / MoO_3 (10 nm) as HIL / Al anode (100 nm). Devices without ZME was also prepared for comparison. All devices were encapsulated with glass lids using epoxy resin to protect active OLED layers from moisture and oxygen exposure. The active emission area of the device was 4.0 mm^2. OLEDs

in conventional architecture with bottom-anode were also fabricated for comparison, according to previously reported procedure [7].

The current density−voltage−luminance ($J-V-L$) characteristics of the devices were measured on a setup combining a source meter (Keithley 2400) and a spectroradiometer (Konica Minolta CS2000). High replicability of 16 devices fabricated in one batch was confirmed by measuring ($J-V-L$) curves which resulted within 1% tolerance. The stability of the device was checked under constant current operation with the initial luminance of 100 cd m^{-2}, employing a EHC CO. Ltd. PEL-100T source meter and a Konica Minolta CS 100A luminance meter. Lifetime (LT50) was defined as time to half the luminance under air with a relative humidity (RH) of 50% at room temperature (25°C). The iOLEDs were also analyzed for their *J-V* characteristics under linear sweep cyclic voltammetry in two terminals, employing a Solartron ModuLab system. The devices were put in a Faraday cage to eliminate noise for measuring sub-nano ampere current. This way, DC capacitance of the devices could be analyzed.

3. Results and discussion

3.1 Thermal conversion of ZME

The ZME precursor films were thermally converted to nc-ZnO under a range of heat treatment conditions. Solution of ZME in 2-ME was spin-coated on a quartz plate at room temperature under dry N_2, heated for 1 h at 30, 60, 100, 130 and 200^{O}C, named as T30, T60, T100, T130 and T200, respectively. Their UV-vis absorption spectra are shown in Figure 1a. While T30 shows an increase of absorption only in a deep UV range below ca. 230 nm, the absorbance in the UV range up to 390 nm gradually increases on increasing the annealing temperature. The associated change of the PL spectra on excitation at 300 nm is shown in Figure 1b. While T30 doesn't show an appreciable PL, increasing the temperature results in an increase of broad emission peak centered at around 470 nm, with its maximum intensity reached for T100. These spectral changes are indicative of nc-ZnO formation by mild annealing. The broadness of the PL peak in the visible range suggests its origin from surface states, not from the nc-ZnO core, as discussed in our previous work [31]. Increasing the temperature above 100°C resulted in a decreased PL intensity and a

corresponding red-shift. T200 gives a weak and broad peak clearly red-shifted to 550 nm, whereas T350 gave almost no luminescence. Full conversion into crystalline ZnO results in defects which are responsible for thermalized loss of excitons.

In order to clarify the chemical state, T30, T100 and T200 samples were characterized by X-ray photoelectron and Auger electron spectroscopies (XPS and AES). The O 1s XPS, Zn LMM AES and C 1s

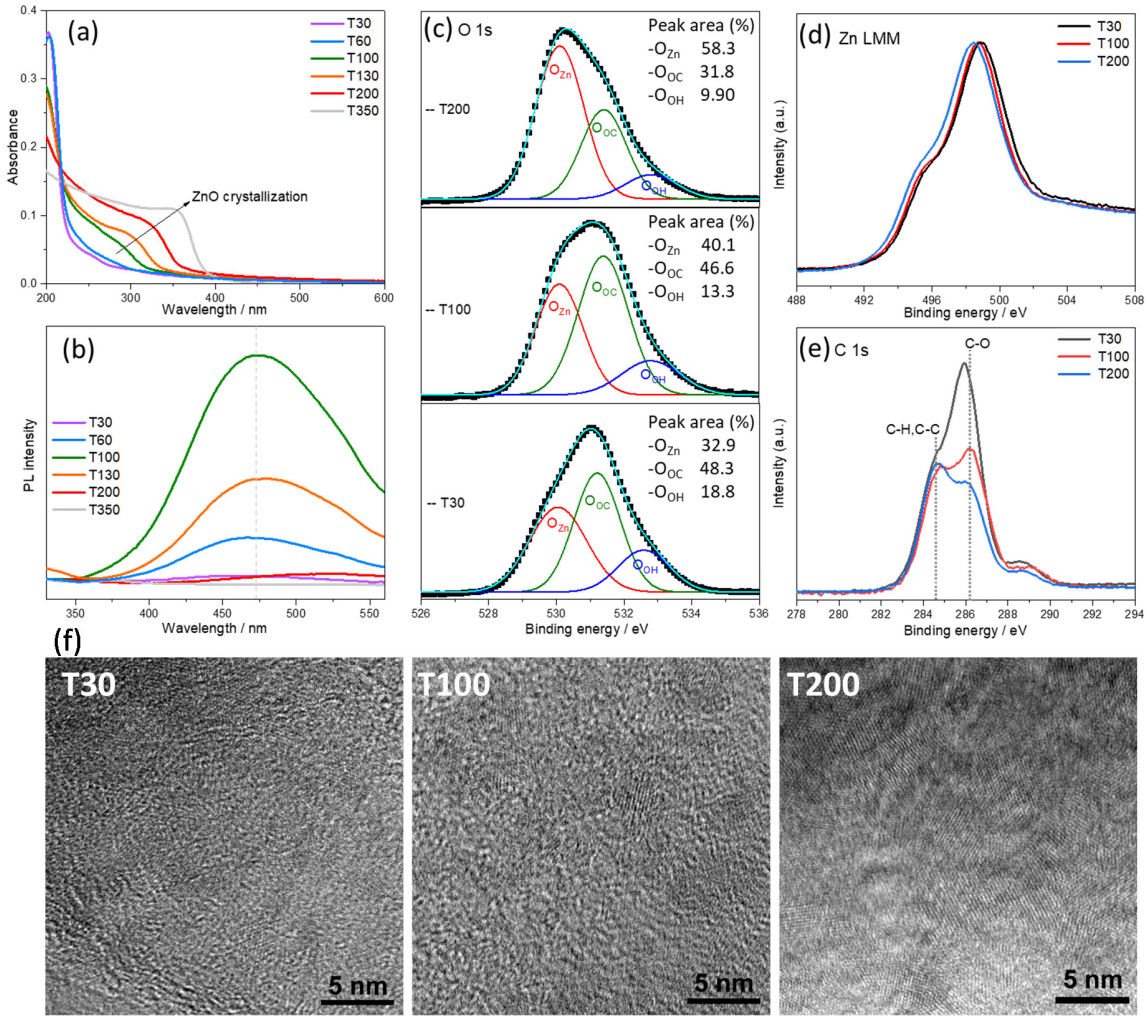

Figure 1. UV-vis absorption spectra (a), PL spectra with λ_{ex} = 300 nm (b), O 1s XPS (c), Zn LMM AES (d) and C 1s XPS (e), high resolution transmission electron microscopic (HR-TEM) images (f) of various ZME layers annealed at various temperatures between 30 and 200ºC under N_2. The sample annealed at 350ºC shown here for reference. The O 1s XPS are deconvoluted into three peaks for which the ratio of peak area was calculated to estimate the chemical composition.

XPS are shown in Figures 1c, d and e, respectively, for the samples prepared on ITO glass substrates. The O 1s XPS (c) can be deconvoluted into three peaks corresponding to Zn-O (530.1 eV), C-O (531.4 eV) and O-H (532.8 eV) [32, 33]. While that of T30 is largely dominated by hydroxide and organic O with large binding energies, increasing the temperature results in their decrease upon increase of Zn-bound O with a small binding energy. At the same time, the Zn LMM AES peak (d) negatively shifts from 498.7 to 498.5 eV, as expected for the formation of ZnO [34]. The main C 1s XPS peak (e) also changes drastically, with its binding energy resolved into 284.6 and 286.2 eV, corresponding to C-C (residual carbon) and C-O (methoxy and alkoxy carbon), respectively [32]. The decrease of the C-O signal with increasing temperature indicates removal of methoxyethoxide ligands upon formation of ZnO. The slight negative shift of the C-O peak by 0.2 eV for T30 can be caused by remaining trace 2-ME solvent in the film. The removal of organic components on increasing the annealing temperature was also supported by ellipsometry of the films prepared on Si substrates (See supporting information Figure S1 for changes of thickness and refractive index of the film on annealing temperature). The ZME layers become thinner and denser by reducing the thickness from 25 nm of T30 to 18 nm of T200, to increase the refractive index due to decomposition of organic ligand on formation of nc-ZnO.

Formation of nc-ZnO was also directly observed in high resolution transmission electron microscopic (HR-TEM) images (Figure 1f). While T30 appears totally amorphous, some crystallized domains are recognized as lattice fringes of nc-ZnO with a few nm diameter in T100. T200, on the other hand, is almost completely converted to nc-ZnO as recognized from the lattice fringes in all over the image.

These observations clearly indicate increasing conversion of ZME to nc-ZnO on increasing the temperature of annealing. While T30 can be considered as simply dried amorphous gel of ZME (ag-ZME), T200 is made mostly of nc-ZnO, and T100 is a mixture of nc-ZnO and ag-ZME. The balance between nc-ZnO and ag-ZME is therefore changed by the annealing temperature. Although increased formation of nc-ZnO resulted in a slight increase of roughness, all layers were highly compact and flat as can be seen in AFM images (Figure S2).

3.2 Performance of iOLEDs

The iOLED devices were fabricated by sequential evaporation of standard stack of organic layers onto various nc-ZnO/ag-ZME layers prepared as above (See supporting information Figure S3 for molecular structure of components, device structure and expected energy diagram) [35,36]. The emission layer (EML) consisted of $Ir(ppy)_3$ diluted in CBP, whereas NBP and NPD were used as electron and hole transport layers (ETL and HTL), respectively. MoO_3 served as a hole injection layer (HIL) onto which Al

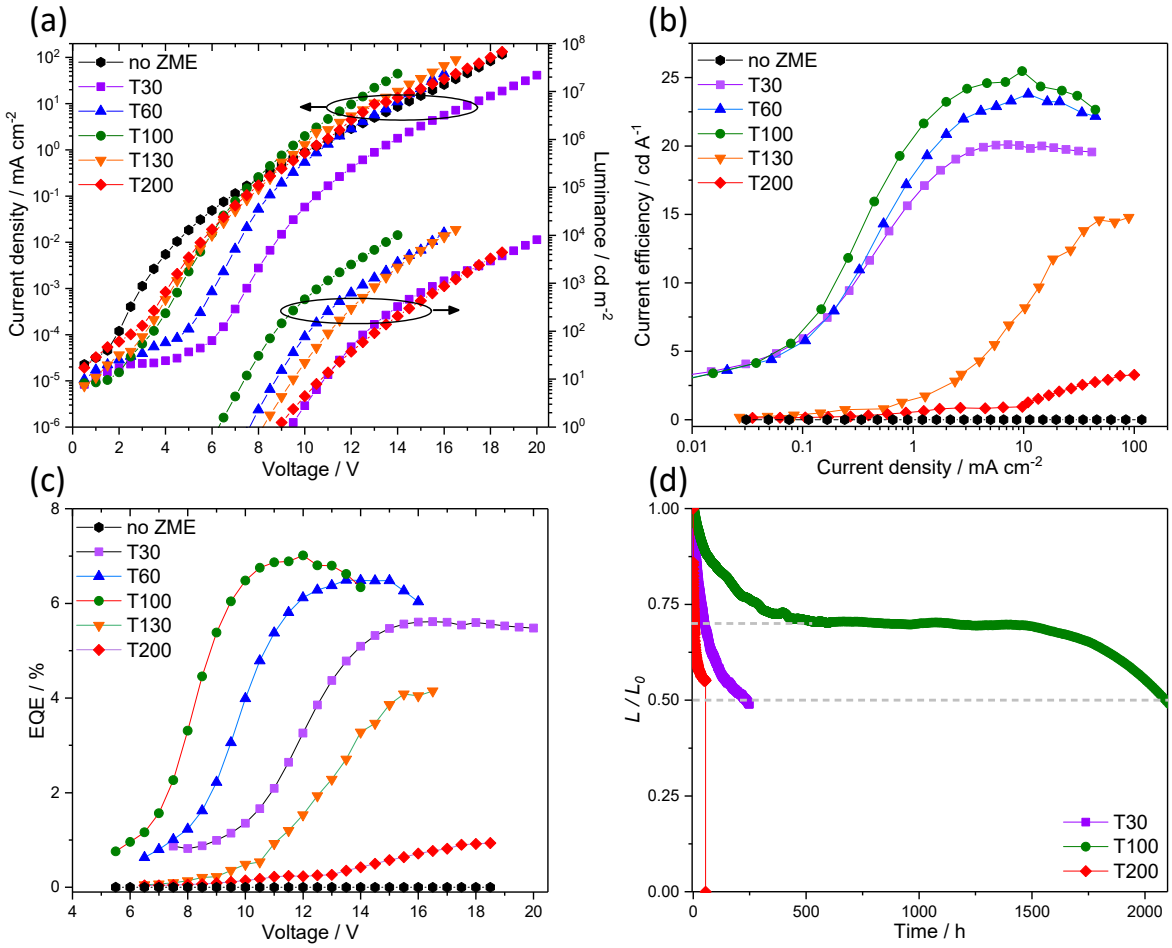

Figure 2. *J-V-L* curves (a), luminance/current vs. *J* curves (b) and external quantum efficiency (EQE) vs. *V* curves (c) of the iOLEDs without EIL and employing T30-200 ZME layers as EIL. Stability test (d) under constant current operation with an initial luminance (L_0) of 100 cd m^{-2} was carried out for iOLEDs employing T30, 100, 200 ZME EILs under air and at room temperature. LT50 was determined as time to half the initial luminance (L/L_0 = 0.5). The operating current density varied as 0.89, 0.81 and 4.06 mA cm^{-2} for T30, T100 and T200 devices, respectively.

was deposited as the top anode.

The performance of thus prepared iOLEDs employing T30, T60, T100, T130 and T200 as EIL is compared in Figure 2. In these devices, current is not limited by hole injection from MoO_3, but by electron injection. Without EIL, interfacial electron-hole recombination at the ITO surface yields large hole-only current and no electroluminescence. When the ZME-based EILs are inserted, all of the devices functioned as iOLEDs with green luminescence expected for $Ir(ppy)_3$ (See supporting information Figure S4 for the spectra of electroluminescence and Table S1 for the device parameters). Current limitation by electron injection to LUMO of NBP was also confirmed in electron-only devices fabricated without EML (See supporting information Figure S5 for the *J-V* curves), for which T200 device gave almost the same *J-V* response as that without EIL, while current was strongly limited by reducing the annealing temperatures down to T30. Thus, electron conduction/injection by ZME limit the current in the complete iOLED devices as well.

While higher processing temperature yields higher injection current at a given voltage, the luminance does not follow the same trend. Plots of the current efficiency of electroluminescence (cd A^{-1}) shows a low efficiency of T200 device, that is significantly improved by reducing the temperature to reach the maximum of roughly 25 cd A^{-1} for T100, nearly ten times greater than the highest observed efficiency for the T200 device. It is remarkable to see even T30 device functions as an efficient iOLED indicating that ag-ZME without nc-ZnO also serves as an EIL. The same trend is also found in the plots of external quantum efficiency (EQE) vs. applied voltage. The maximum EQE of 7.01% achieved for the iOLED employing T100 EIL equals to that achieved with the optimized vacuum-processed OLED in conventional architecture using the same EML (See supporting information Figure S6 for comparison of *J-V-L* curves and EQE plots between conventional and inverted OLEDs). There is an apparent optimum balance between nc-ZnO and ag-ZME to achieve the best performance as an EIL for iOLEDs. Strong conversion of ZME into nc-ZnO by heating at 200°C was detrimental, while raw ag-ZME was also not optimal. Partially converted nc-ZnO/ag-ZME hybrid films yielded the best device efficiency.

Long-term stability under constant current operation for the initial luminance of 100 cd m^{-2} was also checked for the T30, T100 and T200 iOLEDs encapsulated with a glass lid. T200 device quickly decayed and turned off after 54 h. Because of its low efficiency, T200 needed about 5 times higher current than the other two to keep the constant luminous intensity and the redundant current caused heating of the materials, shortening the lifetime. T100, on the other hand, showed a good stability to last for more than 2,000 h until it reduces its luminance to half. T30 was better than T200, but halved its luminance after 236 h. Even though the current was rather small, remaining 2-ME solvent as discussed from its XPS data (see above) could degrade its performance. Nevertheless, a good stability of T100 device is evidence of the practical utility of nc-ZnO/ag-ZME hybrid layer in iOLEDs. It is reasonable to find the highest stability for the device with the highest EQE, as it suffers less from excess Joule heating.

3.3 iOLEDs employing Ca(II) methoxyethoxide (CME)

The high performance of nc-ZnO/ag-ZME hybrid layer may seem counterintuitive as ag-ZME should be electrically resistive while nc-ZnO can be quite conductive. Although nc-ZnO did conduct to cause a high leakage current, it appears that conductivity is not a limiting factor for the efficient "turn-on" of iOLEDs. The presence of ag-ZME obviously plays an important role for efficient electron injection, while preventing non-radiative recombination. The reasonably efficient performance of the T30 device with only ag-ZME raises the question as to the necessity of nc-ZnO.

We therefore employed methoxyethoxide complex of Ca(II) (CME) to produce its amorphous gel layer (ag-CME) by mild heat treatment. Unlike ZME, there is no evidence of crystallization into corresponding oxide (nc-CaO) in the absorption spectra, except that a high temperature annealing at 350°C resulted in removal of organic components (See supporting information Figure S7 for the absorption spectra of CME layers annealed between 30 and 350°C). Therefore, they can be seen as ag-CME up to 200°C.

As shown in Figure 3, the ag-CME indeed worked as an EIL in iOLED, although it had to be kept very thin (5 nm). A device with a thick (25 nm) CME almost did not allow current to flow due to its higher

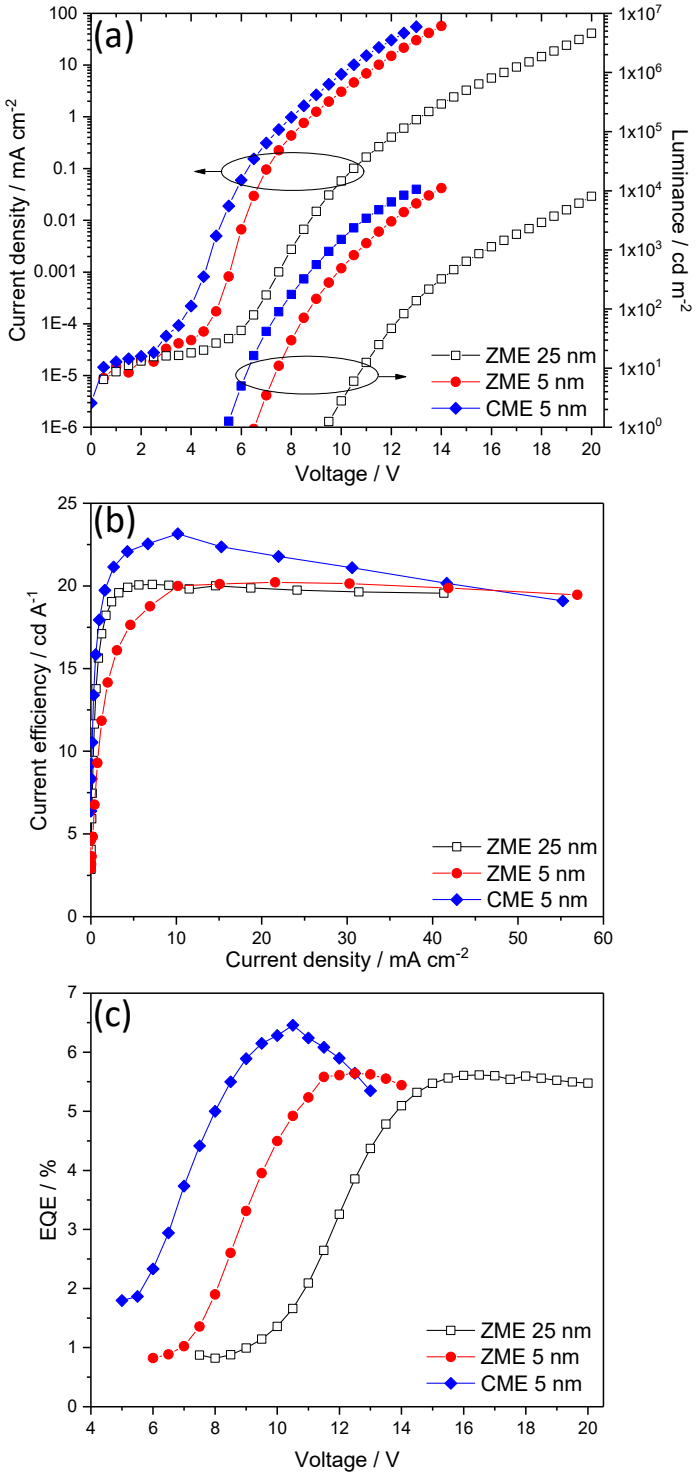

Figure 3. *J-V-L* curves (a), luminance/current vs. *J* curves (b) and external quantum efficiency (EQE) vs. *V* curves (c) of the iOLEDs employing ag-CME (5 nm), thick (25 nm) and thin (5 nm) ag-ZME as EILs. The annealing temperature was 30ºC (T30) both for CME and ZME.

resistance than ZME. The performance of the device with a thin CME is comparable with those

employing ag-ZME. In fact, ag-ZME (T30) device shown for comparison could also significantly reduce its operating voltage by reducing the thickness from 25 to 5 nm. These results indicate high bulk resistance of these amorphous gel layers to impose relatively high turn-on voltages, but does not hinder electron injection. In fact, both ag-ZME and ag-CME contribute to efficient electron injection as recognized from sharp increase of luminance/current efficiency at low current density, while blocking non-radiative recombination current that does not contribute to electroluminescence.

The device parameters determined for all these devices are summarized in Table S1. For sake of comparison, the turn-on voltage was determined according to the definition (V_{on} = voltage at the luminance of 1 cd m^{-2}). Those of iOLEDs employing ag-ZME and ag-CME in the range between 5 and 9 V may appear much larger than that (V_{on} = 4.4 V) of the optimized vacuum-processed OLED in conventional architecture. However, the big gap (ΔV = 7.6 V) between the threshold voltage (V_{th} = 1.2 V) and V_{on} = 8.8 V for T200 device is caused by current leakage via intraband defect states of nc-ZnO. On the other hand, electron conduction through ag-ZME and ag-CME should take place via vacant 4s orbitals of Zn(II) and Ca(II). The presence of conductive nc-ZnO in well-performing devices such as T100 ZME could contribute to achieve a reasonably small V_{on} = 6.2 V.

3.4 Dielectric behavior of ag-ZME

The ag-ZME layers exhibit a high capacitance. Figure 4a shows cyclic voltammograms (CVs) of the iOLEDs employing T30, T100, T130 and T200 ZME, measured at a scan rate of 20 mV s^{-1}. The large gap between positive- and negative-going scans is caused by capacitive charging and discharging current. Fully charging the interface took as long as a minute, as recognized from the time needed for current to go down to zero in chronoamperometric measurements on voltage stepping (See supporting information Figure S8 for the chronoamperograms). On applying a voltage, ag-ZME undergoes slow dielectric polarization, probably due to its structural flexibility and ionicity [29, 37, 38]. One can also recognize small humps both for charging and discharging, which appear at around 3 V for T30 and move towards

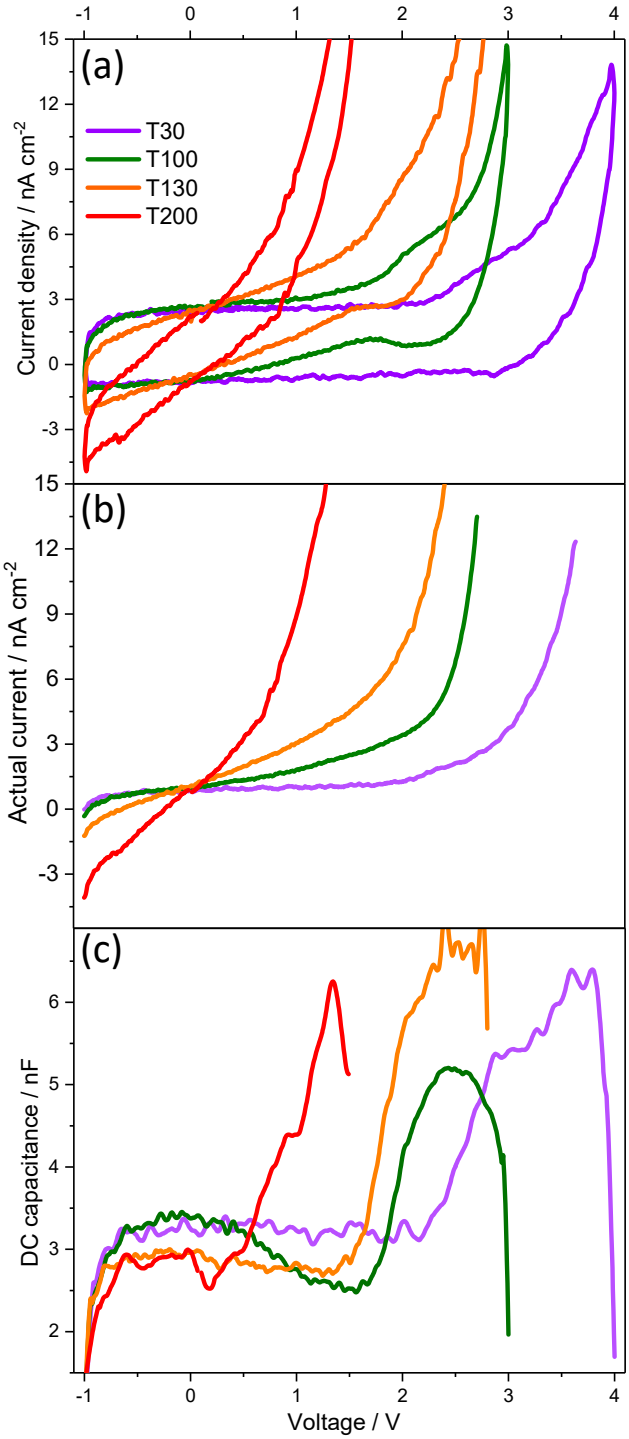

Figure 4. Two-terminal cyclic voltammograms (a, CVs) measured at a scan rate of 20 mV s^{-1} up to the voltage of current onset for the iOLEDs employing T30, 100, 130 and 200 ZME EILs. The profiles of actual current (b) were obtained by averaging current for positive- and negative-going scans of the CVs to cancel out charging/discharging current, whereas the profiles of DC capacitance (c) were obtained by converting CVs to $\Delta Q/\Delta V$.

smaller voltages, around 2.3 V for T100, 2.0 V for T130 and almost disappear for T200. They are most likely related to electron trapping and de-trapping at ag-ZME/NBP boundary [39].

By averaging current for positive- and negative-going scans to cancel out charging and discharging current, we can get a profile of actual current flowing through the device (Figure 4b). It is remarkable to see a total flatness of the curve up to about 2 V for T30, indicating no leakage and ohmic current owing to the high compactness and resistivity of ag-ZME, respectively. The applied voltage only results in a dielectric polarization of the T30 ag-ZME layer and allows only very small ohmic current to flow through the device in this range. The ohmic current gradually increases on increasing the annealing temperature due to decrease of DC resistance of the ZME layer by formation of nc-ZnO. The non-rectified linearly changing current for T200 device is likely caused by shorting.

The charging and discharging current can be converted to DC capacitance of the device as shown in Figure 4c. While the capacitance resulting from dielectric charging/discharging of ag-ZME, close to 0 V, appear in the order as T30 = T100 > T130 = T200, the additional capacitance due to electron trapping and de-trapping is prominent for all of them, but appear at decreasing voltages as T30 > T100 = T130 > T200. It is important to note about the coincidence between voltage for completion of electron trapping and that for the onset of actual current. When the electron traps are filled, the electrons percolate from the ZME layer to the EML.

Very similar capacitive behavior was observed in the CV measurements on iOLEDs employing ag-CME (See supporting information Figure S9 for CVs, actual current and DC capacitance plotted against voltage, for the iOLEDs employing ag-CME in comparison with those employing a thin (5 nm) ZME, annealed at 30 or 200°C). Dielectric capacitance due to slow polarization of ag-CME as well as additional rise by interfacial electron trapping were recognized. Increased temperature to 200°C gave marginal effects for CME as it could not be converted to conductive oxides. It is also recognized that thinning of ag-ZME

results in reduced voltage for the bumps of electron trapping and for the onset of actual current due to decrease in resistance.

3.5 Role of EIL in iOLEDs

Our experimental exploration in solution processing of EILs for iOLEDs led us to the understanding of functionality of EIL as visually presented in Figure 5. When devices were fabricated without ZME layer, by directly depositing the OLED stack on ITO, high current was observed but resulted in no emission. Heavily doped ITO is metallic, so that hole in the EML injected from MoO_3 top contact is directly reduced, while electron injection from ITO to the EML is not expected. This way, "hole-only" current flows through the device as illustrated in Fig. 5a. EILs are therefore needed for hole-blocking and to achieve electron injection to the EML. Ideally, semiconducting ZnO should be able to take this role, as

its conduction band edge (~ 4.0 eV vs. VAC [13, 27]) is well aligned with the LUMO of NBP (~ 2.8 eV vs. VAC [35]) in the static energy diagram. Furthermore, the high electron mobility of ZnO suggest that it could be a high-performance EIL. The nc-ZnO layers processed from ZME by annealing at relatively high temperatures (T130, T200) did achieve electron injection to the emitting layer, and thereby

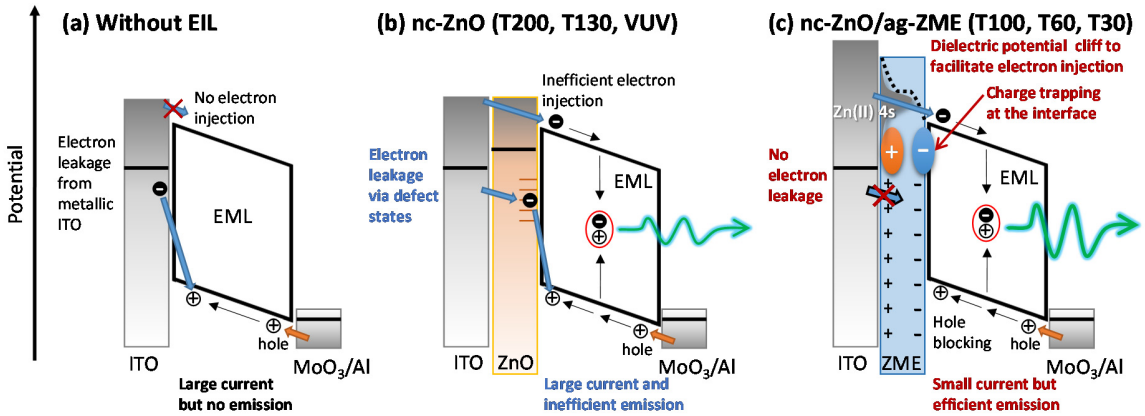

Figure 5. Schematics of the role of EILs in iOLEDs. (a) Without an EIL, (b) with nc-ZnO EILs (T200, T130 ZME), and (c) with nc-ZnO/ag-ZME EILs (T100, T60, T30 ZME).

electroluminescence as illustrated in Fig. 5b. However, non-radiative current leakage turned out to be responsible to the observed large current and low efficiency. As we promote crystallization of ZME into ZnO, defects are generated providing interfacial recombination centers. Therefore, such devices suffer from low current efficiency and short lifetime because the redundant current by leakage only heats up the material.

Major improvements were then achieved with ag-ZME. Its functionalities are best understood by the behavior of T30 device as illustrated in Fig. 5c. It is highly compact and resistive to prevent interfacial electron-hole recombination current. When a voltage is applied to the device, however, ag-ZME undergoes dielectric polarization to build up a potential step between ITO and the emitting layer. This step acts much like the electrical double layer to facilitate electron transfer in electrochemical events [40]. However, the contact of ag-ZME with NBP also results in electron traps, which appeared as humps just before the onset of actual current in the CVs. When the traps are filled, electrons can percolate for efficient electron injection to EML. This way, high luminance/current efficiency was achieved with ag-ZME, right following its turn-on. Electron transport within ag-ZME is expected to occur via narrowly distributed 4s orbital of Zn(II) that acts as a gate of electron for its selective injection to EML. This proposed mechanism for electron injection is supported by the achievement of equally good performance of ag-CME, which is even less conductive than ag-ZME but also offers 4s orbitals of Ca(II).

The high resistivity of ag-ZME did limit current and imposed relatively large V_{on}, so that T30 ag-ZME and ag-CME had to be kept very thin. Also, the device with a thick T30 ag-ZME had a limited lifetime, most likely due to the presence of residual 2-ME solvent in the layer. However, they were greatly improved by partial conversion of ag-ZME to conductive nc-ZnO with slightly increased annealing temperature. T100 appears to find an optimal balance between nc-ZnO and ag-ZME in their hybrid structure to achieve a high performance and a long lifetime.

4. Conclusions

Uniformly flat and highly compact nc-ZnO/ag-ZME hybrid layers were processed by solution coating of ZME precursor and mild annealing under N_2. They were proven to work as good EILs in iOLEDs to achieve high current efficiency (25.5 cd A^{-1}), EQE (7.01%) and long operational lifetime (LT50 > 2000 h) with the best example of T100 device in the optimum balance of nc-ZnO and ag-ZME. The EILs largely converted to ZnO by annealing with increased temperatures worked poorly. They are not ideal ZnO but those with defects, which act as paths for non-emissive current leakage.

The discovery of dielectric behavior of ag-ZME suggests an operational principle for design of EILs in iOLEDs. Rather than the absolute conductivity, dielectric polarization and ability to gate electrons with suitably located, narrowly distributed state density seem to matter. In fact, the need of organic modifiers applied to ZnO surface in the previous studies [19, 26, 29, 30] may also be for the same reasons.

This principle is demonstrated in both ZME and CME, and potentially applicable to a variety of metal-organic complexes where similar or better performance may be discovered. Processing of such EILs can be achieved by solution coating and at low temperatures, compatible with flexible substrates and this new strategy to design amorphous dielectric metal-organic (ADMO) EIL may yield high performance, flexible and stable electronic devices, such as iOLEDs and perovskite solar cells.

Supporting Information

Changes of film thickness and refractive index of ZME layer on the annealing temperature (Figure S1), Atomic Force Microscopy (AFM) images of ZME layers prepared after annealing at various temperatures (Figure S2), Structures of organic molecules used, device structure and energy diagram of the iOLED in this study (Figure S3), Normalized electroluminescence spectra of iOLEDs with various ZME EILs at a luminance of 100 cd m-2 (Figure S4), The device configuration of electron-only devices (EODs) and *J-V* curves of EODs with ZME EILs prepared by different annealing temperature (Figure S5), Comparison of *J-V-L* curves and EQE vs. current density curves between conventional and inverted OLEDs (Figure S6), UV-vis transmission absorption spectra of the CME layers annealed at various temperatures (Figure S7), Chronoamperograms for dielectric charging and discharging of iOLED devices employing various ZME as EILs upon voltage stepping (Figure S8), Cyclic voltammograms (CVs) measured for the iOLEDs employing 5 nm thin EILs of ZME and CME layers annealed at 30 or 200ºC (T30 or T200), the profiles of DC current passing through the device by averaging current and the profiles of DC capacitance were obtained by converting CVs to $\Delta Q/\Delta V$ (Figure S9), The device performance for the OLEDs prepared and measured in this study (Table S1).

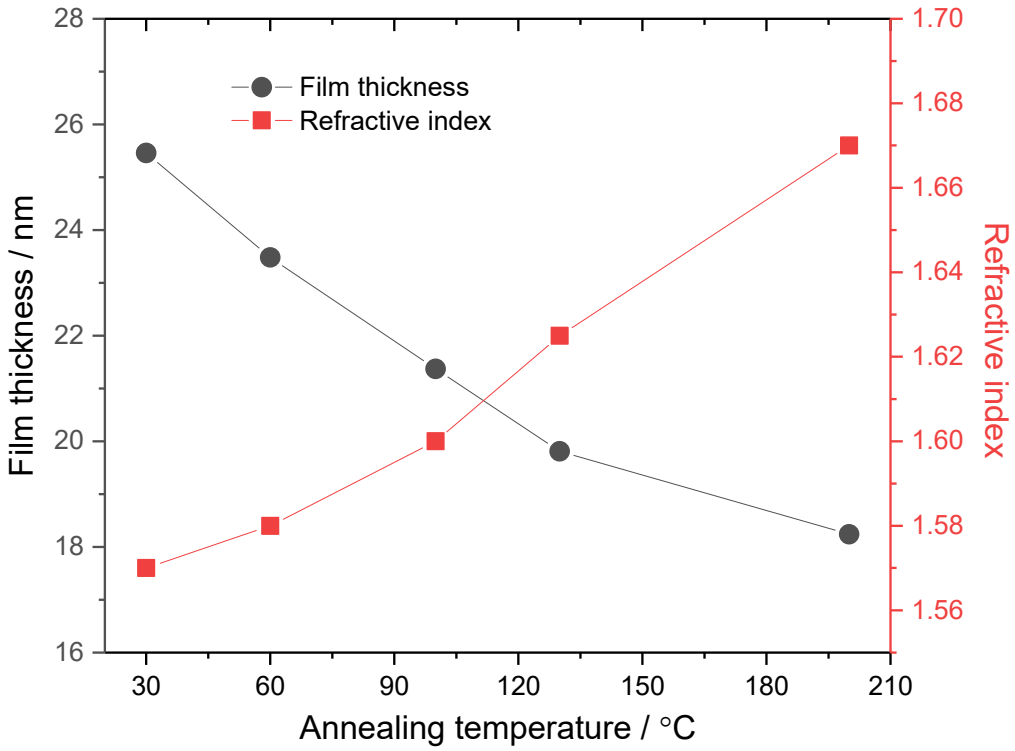

Figure S1 Changes of film thickness and refractive index of ZME layers on the annealing temperature, as determined by ellipsometry.

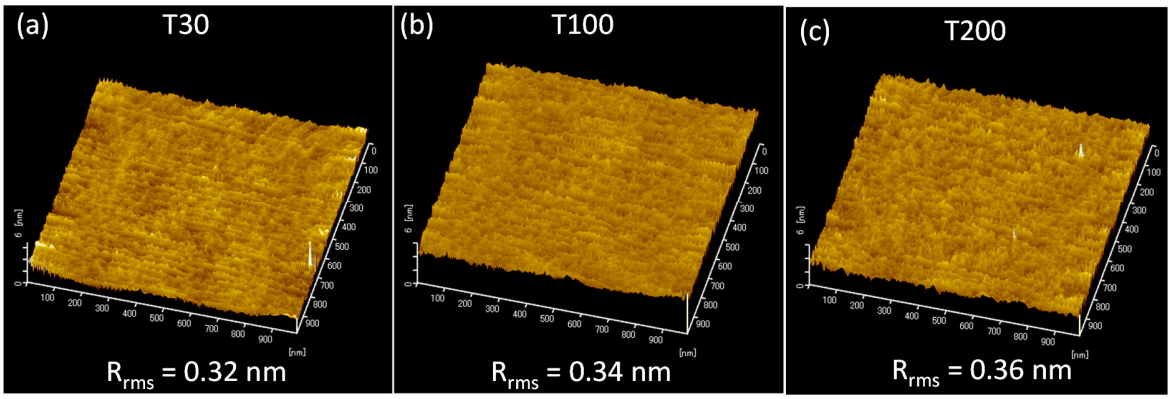

Figure S2 Atomic Force Microscopy (AFM) images of ZME layers prepared after annealing at various temperatures of 30, 100 and 200ºC under N_2.

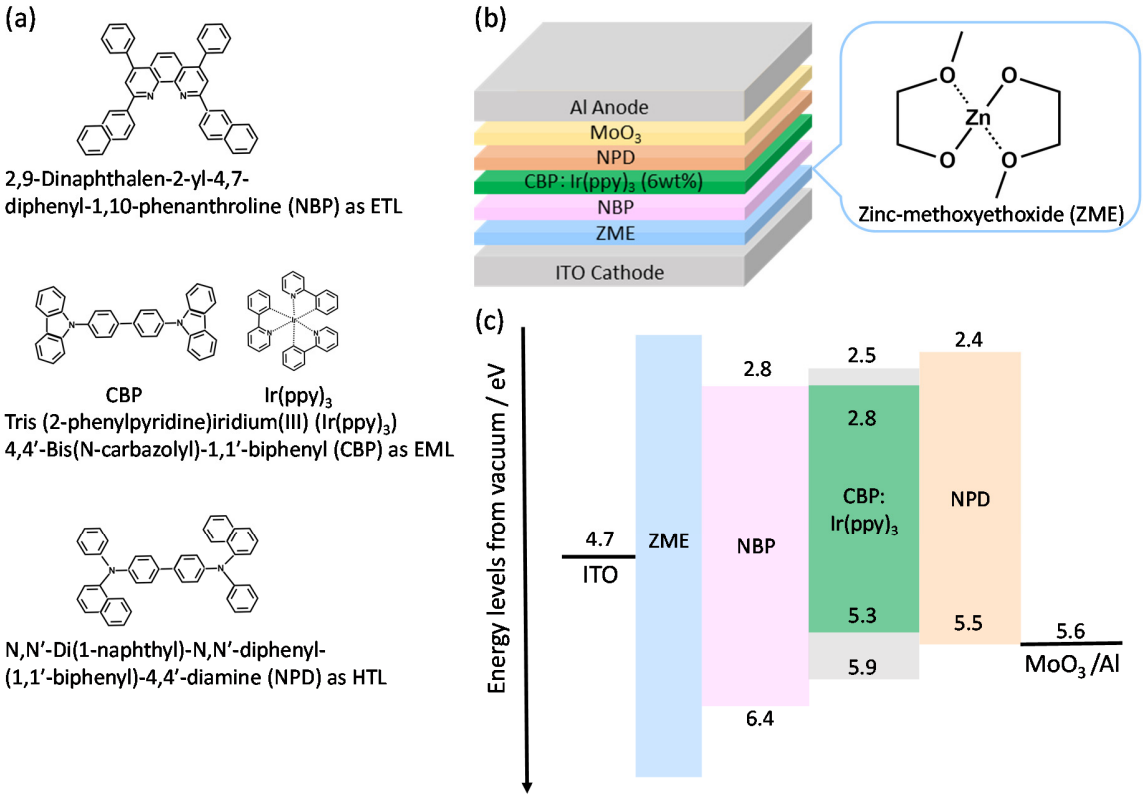

Figure S3 Structures of organic molecules used as ETL, EML and HTL (a), device structure (b) and energy diagram (c) of the iOLED in this study.

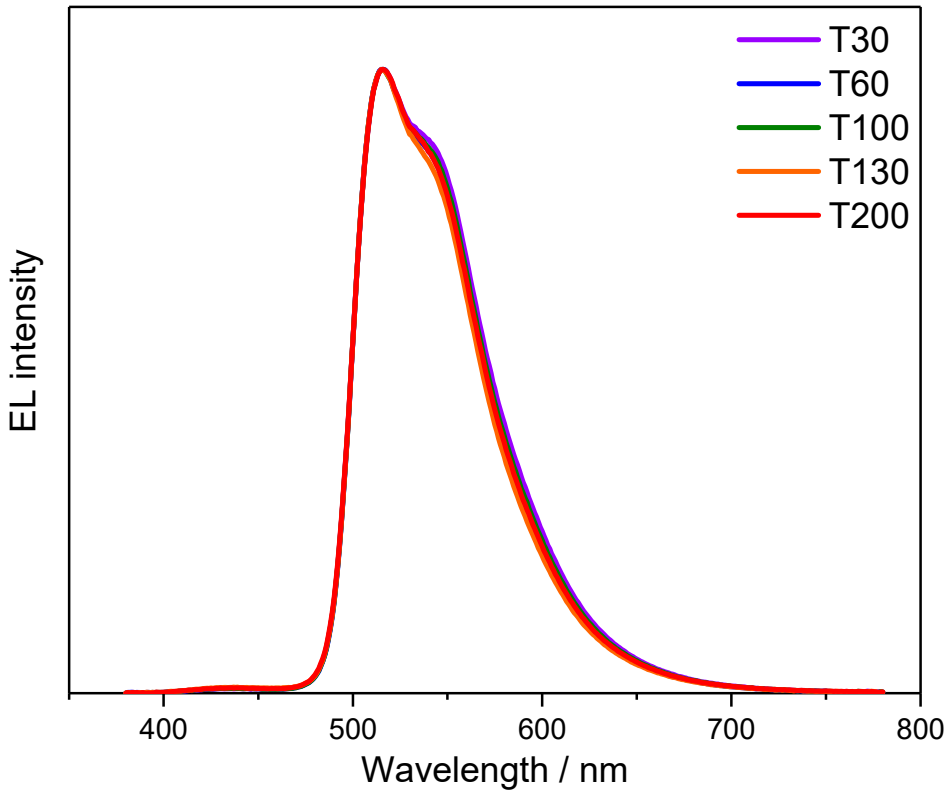

Figure S4 Normalized electroluminescence spectra of iOLEDs with T30, T60, T100, T130 and T200 ZME EILs at a luminance of 100 cd m^{-2}.

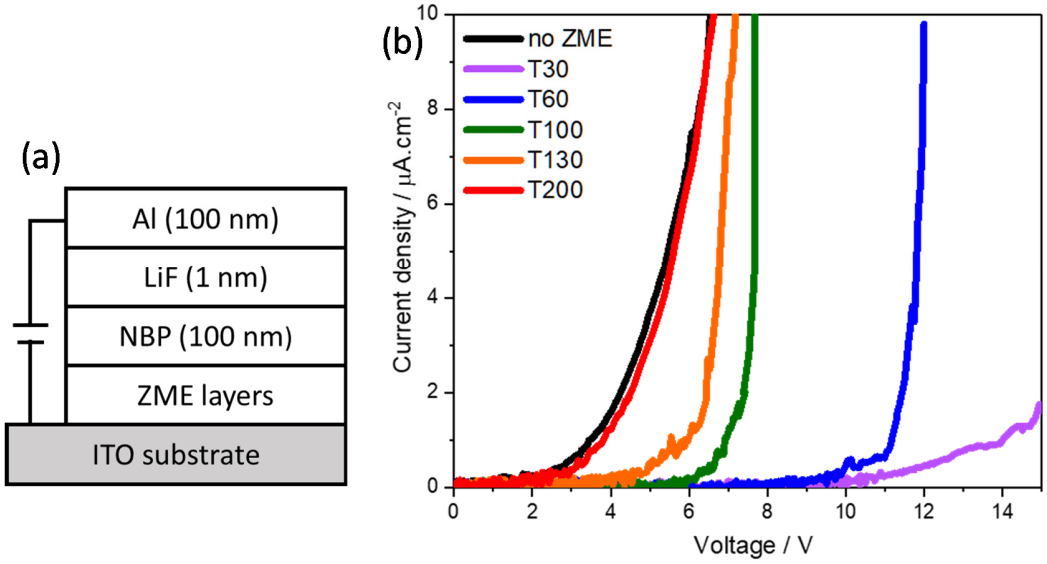

Figure S5 (a) The device configuration of electron-only devices (EODs) with structure of ITO/ZME/NBP/LiF/Al. and (b) *J-V* curves of EODs with ZME EILs prepared by different annealing temperature.

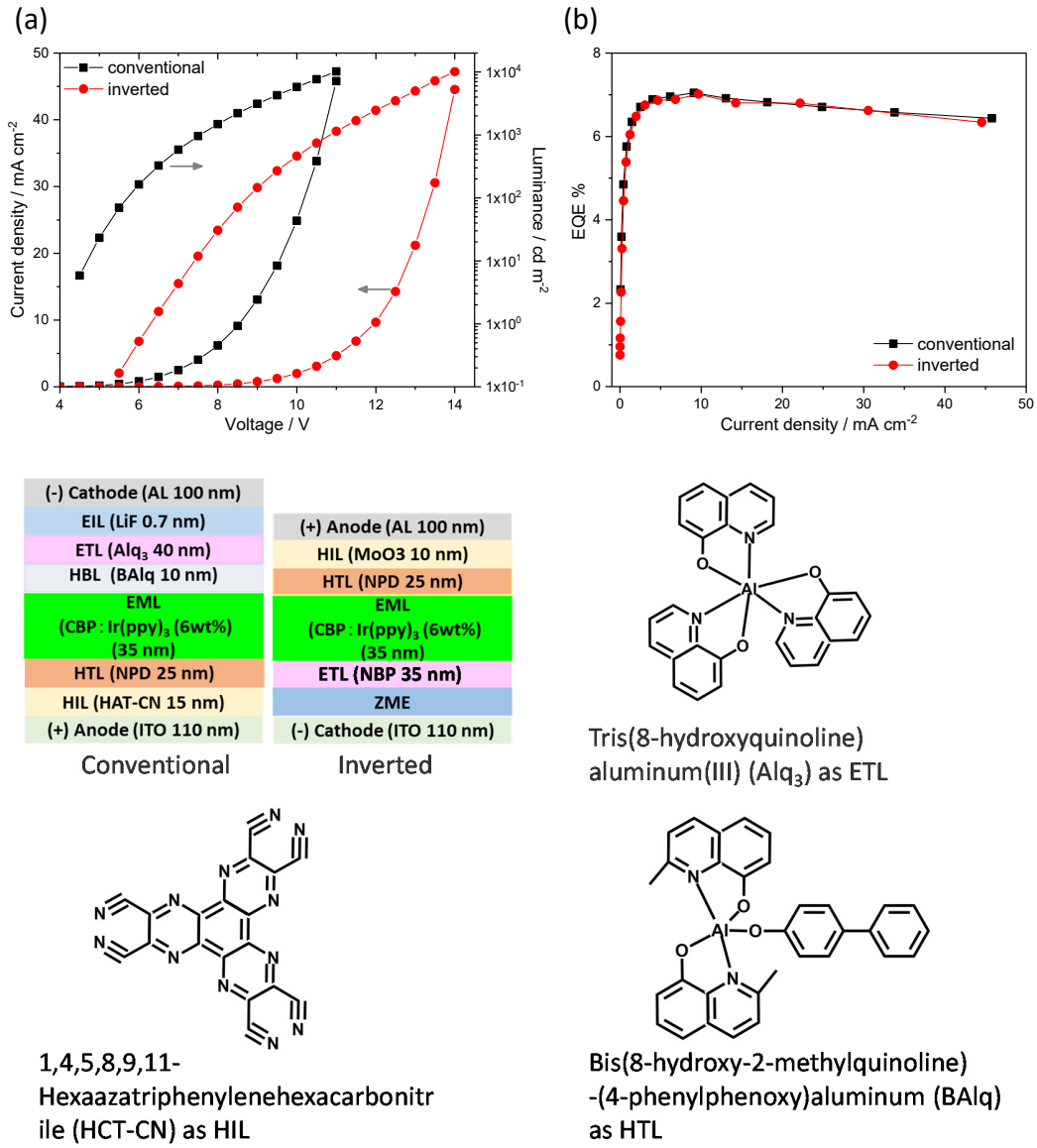

Figure S6 Comparison of *J-V-L* curves (a) and EQE vs. current density curves (b) between conventional and inverted OLEDs. The same EML as the iOLED, but with optimized components for EIL, ETL, HTL and HIL are used for the conventional OLED as shown in the drawing. Except the increased voltage of operation, the iOLED with solution processed T100 ZME achieves the same high efficiency as the vacuum-processed OLED.

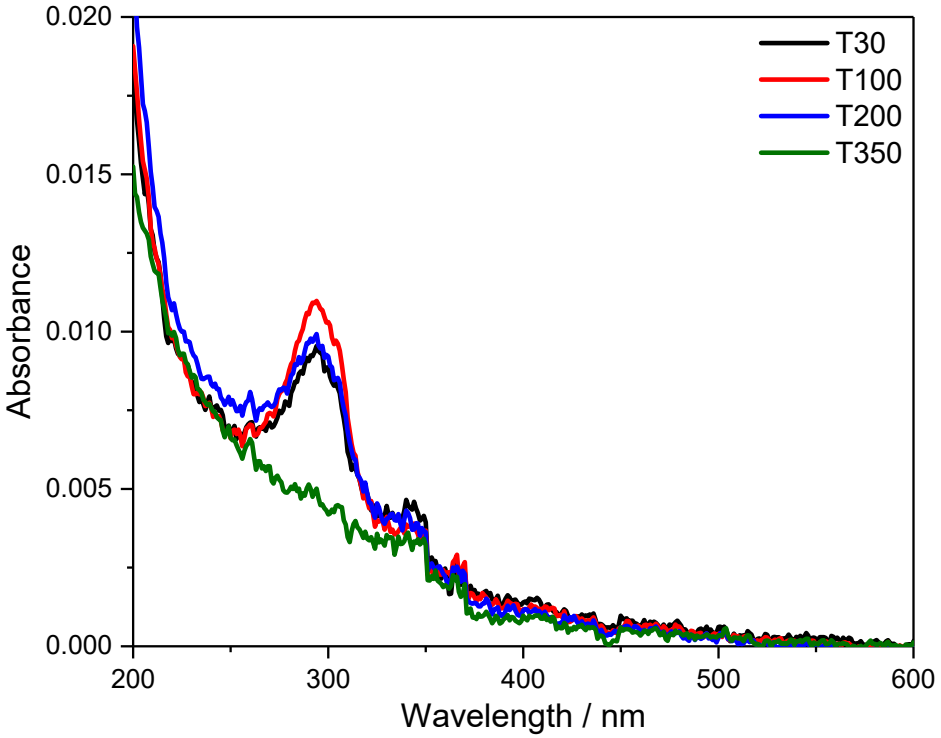

Figure S7 UV-vis absorption spectra of the CME layers coated on quartz glass substrates and annealed at 30, 100, 200 and 350°C under N_2.

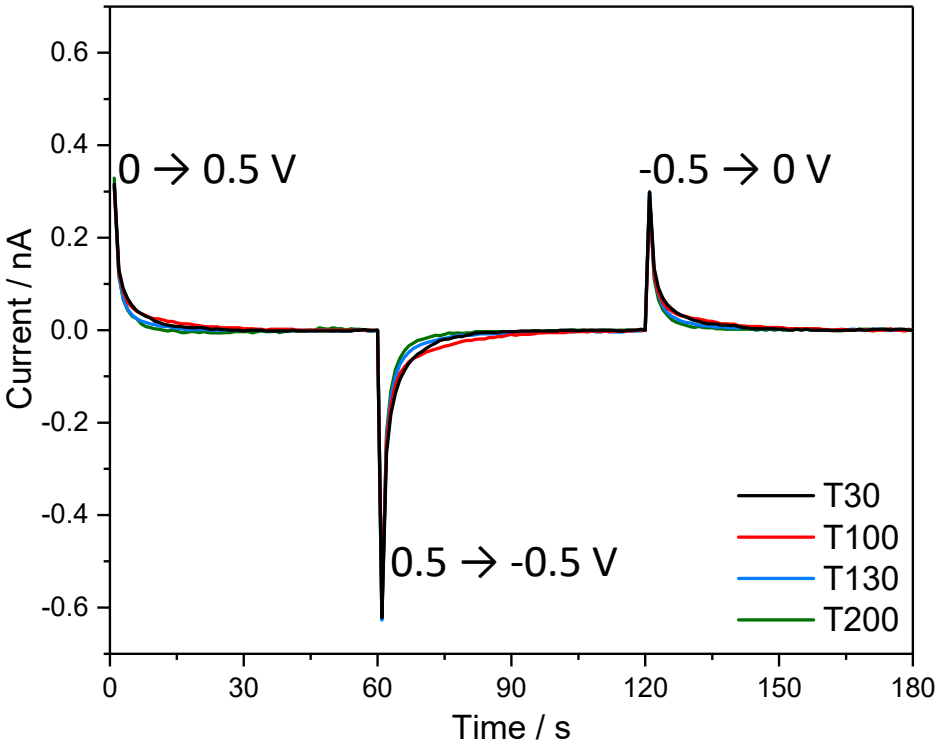

Figure S8 Chronoamperograms for dielectric charging and discharging of iOLED devices employing T30, T100, T130 and T200 ZME as EILs upon voltage stepping. Note the slowness of charging/discharging that takes for tens of seconds to be completed.

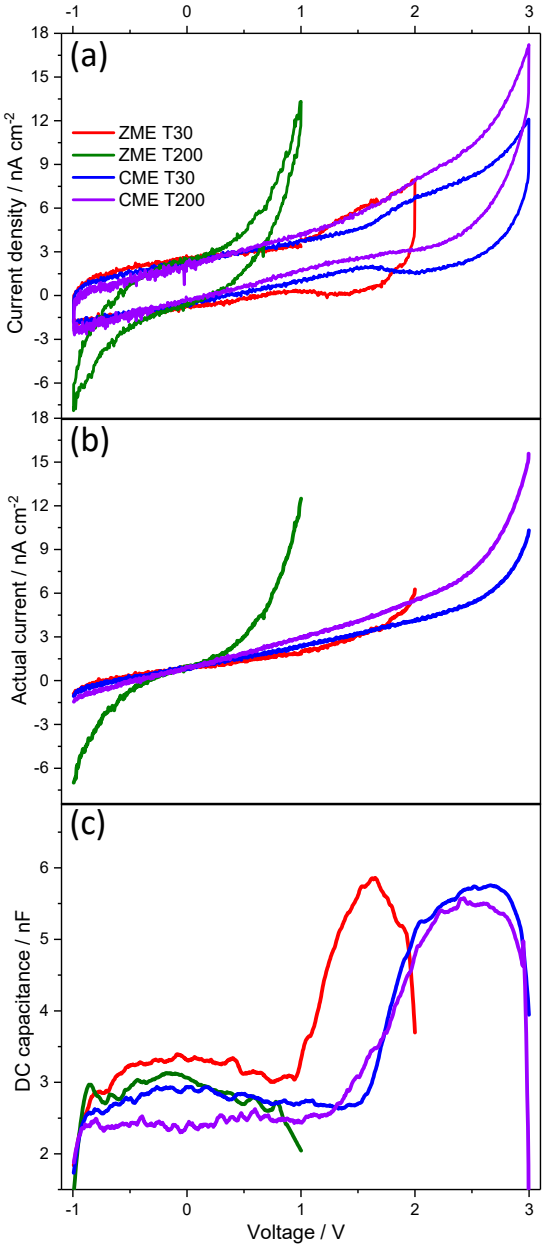

Figure S9 Two-terminal cyclic voltammograms (a, CVs) measured at a slow scan rate of 20 mV s^{-1} up to the voltage of current onset for the iOLEDs employing 5 nm thin EILs of ZME and CME layers annealed at 30 or 200ºC (T30 or T200). The profiles of actual current flowing through the device (b) were obtained by averaging current for positive- and negative-going scans of the CVs to cancel out charging/discharging current, whereas the profiles of DC capacitance (c) were obtained by converting CVs to $\Delta Q/\Delta V$.

Table S1 The device performance according to the standard definitions for the OLEDs prepared and measured in this study; [a]V_{th} is defined as the threshold voltage where the charge injection begins to rise, determined from extrapolation of linear fitting of log$J$ to the voltage scale; [b]V_{on} is defined as the voltage at the luminance of 1 cd m^{-2}; [c]EQE is external quantum efficiency; [d]CE is the efficiency of luminance (cd) / current (A).

EIL	V_{th}[a] / V	V_{on}[b] / V	LT50 / h	Max. EQE[c] / %	Max. CE[d] / (cd A^{-1})	@ 1000 cd m^{-2}	
						V / V	J / (mA cm^{-2})
T30	4.0	9.33	236	5.62	20.09	15.76	5.00
T60	3.0	7.58		6.49	23.80	12.60	4.41
T100	2.0	6.23	2100	7.01	25.47	10.81	4.06
T130	1.6	8.14		4.15	14.77	13.16	11.38
T200	1.2	8.79	54	0.94	3.33	16.19	37.82
Conventional OLEDs	2.0	4.42		6.96	24.30	7.53	4.18
ZME (5 nm)	2.5	6.51		5.64	20.21	10.69	5.50
CME (5 nm)	2.0	5.38		6.46	23.15	9.55	4.51

Author contributions

L. S. performed the sample preparation and characterization of the materials and devices, and all measurements. L. S. and T. Y. analysed the data and co-wrote the manuscript. Y. H. carried out the measurement of DC capacitance and analysis. M. W. contributed to the discussion about electron injection mechanism and manuscript revisions. Y. S. participated in its design and conceived the study.

Conflicts of interest

There are no conflicts to declare.

Acknowledgements

This work was financially supported by Grant-in-Aid for JSPS Research Fellow JP 20J40137, JSPS KAKENHI Grant Number JP 20K05317 and JSPS Partnerships for International Research and Education (PIRE) Grant Number JPJSJRP20221201. This material is based upon work supported by the National Science Foundation under Grant No. OISE-2230706. The JSPS and NSF grants represent complementary funding in support of "US-Japan Partnership in Excitonic Soft Materials for Clean Energy". The work was also supported by Yamagata University Center of Excellence (YU-COE) Collaboration Program and Yamagata University Carbon Neutral Research Center (YUCaN). The authors thank Ms. A. Shimokawa (Sumika Chemical Analysis Service, Ltd.) for XPS measurements.

References

1. J.H. Burroughes, D.D.C. Bradley, A.R. Brown, R.N. Marks, K. Mackay, R.H. Friend, P.L. Burns, A.B. Holmes, Light-emitting diodes based on conjugated polymers, Nature, 347 (1990) 539–541.

2. M. C. Gather, A. Köhnen, and K. Meerholz, White Organic Light-Emitting Diodes. Adv. mater. 23 (2011) 233.

3. M.S. White, M. Kaltenbrunner, E.D. Głowacki, K. Gutnichenko, G. Kettlgruber, I. Graz, S. Aazou, C. Ulbricht, D.A. Egbe, M.C Miron, Z. Major, Ultrathin, Ultrathin, Highly Flexible and Stretchable PLEDs. Nat. Photonics. 7 (2013) 811-816.

4. T. Chiba, Y.-J. Pu, J. Kido, Solution-Processed White Phosphorescent Tandem Organic Light-Emitting Devices. Adv. Mater. 27 (2015) 4681.

5. S. Wang, H. Zhang, B. Zhang, Z. Xie, W. Wong, Towards High-Power-Efficiency Solution-Processed OLEDs: Material and Device Perspectives. Mater. Sci. Eng. R Rep. 140 (2020) 100547.

6. Y. Duan, Y. Yang, Z. Chen, Y. Tao, Y. Liu, Recent Progress on Thin-Film Encapsulation Technologies for Organic Electronic Devices. Opt. Commun. 362 (2016) 43-49.

7. L. Sun, Y. Kurosawa, H. Ito, Y. Makishima, H. Kita, T. Yoshida, Y. Suzuri, Solution Processing of Alternating PDMS/SiOx Multilayer for Encapsulation of Organic Light Emitting Diodes, Org. Electron. 64 (2019) 176-180.

8. L. Sun, Y. Kurosawa, T. Yoshida and Y. Suzuri, Vacuum Ultraviolet Photochemical Sol-Gel Processing of Zn, Sn, Zn-Sn Oxide Thin Films for Encapsulation of Organic Light Emitting Diodes, J. Electrochem. Soc. 166 (2019) B3176-B3183.

9. L. Sun, K. Uemura, T. Takahashi, T. Yoshida, Y. Suzuri, Interfacial Engineering in Solution Processing of Silicon-Based Hybrid Multilayer for High Performance Thin Film Encapsulation, ACS Appl. Mater. Interfaces, 11 (2019) 43425-43432.

10. P. C. With, U. Helmstedt, L. Prager, Flexible Transparent Barrier Application of Oxide Thin Films Prepared by Photochemical Conversion at Low Temperature and Ambient Pressure. Front. Mater. 7 (2020) 1-13.

11. M. Schaer, F. Nüesch, D. Berner, W. Leo, L. Zuppirol, Water Vapor and Oxygen Degradation Mechanisms in Organic Light Emitting Diodes. Adv. Funct. Mater. 11 (2001) 116-121.

12. K. Moriia, M. Ishida. Encapsulation-free hybrid organic-inorganic light-emitting diodes. Appl. Phys. Lett. 89 (2006) 183510.

13. H.J. Bolink, E. Coronado, J. Orozco, M. Sessolo, Efficient Polymer Light-Emitting Diode Using Air-Stable Metal Oxides as Electrodes. Adv. Mater. 21 (2009) 79-82.

14. H. Fukagawa, K. Morii, M. Hasegawa, Y. Arimoto, T. Kamada, T. Shimizu, T. Yamamoto, Highly efficient and air-stable inverted organic light-emitting diode composed of inert materials. Appl. Phys. Exp. 7 (2014) 082104.

15. S. Liu, C. Zang, J. Zhang, S. Tian, Y. Wu, D. Shen, L. Zhang, W. Xie, C. Lee. Air-Stable Ultrabright Inverted Organic Light-Emitting Devices with Metal Ion-Chelated Polymer Injection Layer. Nano-Micro Lett. 14 (2022) 14.

16. S.N. Hsieh, S.P. Chen, C.Y. Li, T.C. Wen, T.F. Guo, Y.J. Hsu, Surface modification of TiO2 by a self-assembly monolayer in inverted-type polymer light-emitting devices. Org. Electron. 10 (2009) 1626.

17. M. Sessolo, H. J. Bolink. Hybrid Organic-Inorganic Light-Emitting Diodes. Adv. Mater. 23 (2011) 1829–1845.

18. R. Kaçar, S. P. Mucur, F. Yıldız, S. Dabak, and E. Tekin, Solution processed ternary blend nano-composite charge regulation layer to enhance inverted OLED performances, Appl. Phys. Lett. 112 (2018) 163302.

19. I. Hamilton, M. Suh, K. Kim, D. Y. Jeon, D. D.C. Bradley, J. S. Kim. Organic-inorganic hybrid composites as an electron injection layer in highly efficient inverted green-emitting polymer LEDs. Org. Electron. 77 (2020) 105496.

20. L. S. Hung, C. W. Tang, M. G. Mason, Enhanced electron injection in organic electroluminescence devices using an Al/LiF electrode. Appl. Phys. Lett. 70 (1997) 152-154.

21. J. H. Kwon, J. Y. Lee, High efficiency and long lifetime in organic light-emitting diodes using bilayer electron injection structure. Syn. Metals, 159 (2009) 1292–1294.

22. H. Ma, H. L. Yip, F. Huang, A. K. Y. Jen, Interface Engineering for Organic Electronics. Adv. Funct. Mater. 20 (2010) 1371.

23. J. Lee, J. Kim. Electron injection and transport for high-performance inverted organic light-emitting diodes. J. Inf. Disp. 14 (2013) 39-48.

24. P. Li, Z. Lu. Interface Engineering in Organic Electronics: Energy-Level Alignment and Charge Transport. Small Sci. 1 (2021) 2000015.

25. Sasaki, T., Hasegawa, M., Inagaki, K. et al. Unravelling the electron injection/transport mechanism in organic light-emitting diodes. Nat Commun. 12 (2021) 2706.

26. Y. Kim, T. Han, H. Cho, S. Min, C. Lee, T. Lee, Polyethylene Imine as an Ideal Interlayer for Highly Efficient Inverted Polymer Light-Emitting Diodes. Adv. Funct. Mater. 24 (2014) 3808–3814.

27. M. Takada, T. Nagase, T. Kobayashi, H. Naito, Electron injection in inverted organic light-emitting diodes with poly(ethyleneimine) electron injection layers. Org. Electron. 50 (2017) 290-295.

28. J. S. Park, B. R. Lee, J. M. Lee, J.-S. Kim, S. O. Kim, M. H. Song, Efficient hybrid organic-inorganic light emitting diodes with self-assembled dipole molecule deposited metal oxides. Appl. Phys. Lett. 96 (2010) 243306.

29. B. R. Lee, H. Choi, J. S. Park, H. J. Lee, S. O. Kim, J. Y. Kim, M. H. Song, Surface modification of metal oxide using ionic liquid molecules in hybrid organic–inorganic optoelectronic devices. J. Mater. Chem. 21 (2011) 2051.

30. C. Li, Y. Chou, J. Syu, S. Hsieh, T. Tsai, C. Wu, T. Guo, W. Hsu, Y. Hsu, T. Wen, Effect of annealing ZnO on the performance of inverted polymer light-emitting diodes based on SAM/ZnO as an electron injection layer. Org. Electron. 12 (2011) 1477–1482.

31. L. Sun, K. Uda, T. Yoshida, Y. Suzuri, Photochemical Conversion of Ethanolamine-Zn^{2+} Complex Gel under Vacuum Ultraviolet Irradiation Associated with Color-Tunable Photoluminescence. J. Phys. Chem. C. 125 (2021) 5417-5424.

32. https://www.thermofisher.com/jp/ja/home/materials-science/learning-center/periodic-table.html (accessed Aug 18, 2022)

33. L. Jiang, J. Li, K. Huang, S. Li, Q. Wang, Z. Sun, T. Mei, J. Wang, L. Zhang, N. Wang, X. Wang, Low-Temperature and Solution-Processable Zinc Oxide Transistors for Transparent Electronics. ACS Omega, 2 (2017) 8990–8996.

34. W. J. Li, L. Fang, G. P. Qin, H. B. Ruan, H. Zhang, C. Y. Kong, L. J. Ye, P. Zhang, and F. Wu, J. Tunable zinc interstitial related defects in ZnMgO and ZnCdO films, Appl. Phys. 117 (2015) 145301.

35. H. I. Baek, C. H. Lee. Optimization of white organic light emitting diodes based on emitting layer charge carrier conduction properties. J. Phys. D: Appl. Phys. 41 (2008) 105101.

36. M. Regnata, K. P. Pernsticha, B. Ruhstaller, Influence of the bias-dependent emission zone on exciton quenching and OLED efficiency. Org. Electron. 70 (2019) 219–226.

37. B. K. Min, S. K. Kim, S. J. Kim, S. H. Kim, M. Kang, C.Y. Park, W. Song, S. Myung, J. Lim. K. An, Electrical Double Layer Capacitance in a Graphene-embedded Al_2O_3 Gate Dielectric. Sci Rep 5 (2015) 16001.

38. J. Guo, T. Bamber, M. Chamberlain, L. Justham, M. Jackson, Optimization and experimental verification of coplanar interdigital electroadhesives. J. Phys. D: Appl. Phys. 49 (2016) 415304.

39. Y. Noguchi, Y. Miyazaki, Y. Tanaka, N. Sato, Y. Nakayama, T. D. Schmidt, W. Brütting, H. Ishii, J. Charge accumulation at organic semiconductor interfaces due to a permanent dipole moment and its orientational order in bilayer devices. Appl. Phys. 111 (2012) 114508.

40. A. J. Bard, L. R. Faulkner, H. S. White, Electrochemical methods: fundamentals and applications. Wiley. 2001. 2nd ed.